Corrosion behaviour of maize husk reinforced aluminium (1070) metal matrix composites in chloride-sulphate solution

To cite this article: Roland Tolulope Loto and Williams Joseph Ajuwaeze 2022 *Mater. Res. Express* **9** 116501

Materials Research Express

PAPER

Corrosion behaviour of maize husk reinforced aluminium (1070) metal matrix composites in chloride-sulphate solution

Roland Tolulope Loto* and **Williams Joseph Ajuwaeze**

Department of Mechanical Engineering, Covenant University, Ota, Ogun State, Nigeria

* Author to whom any correspondence should be addressed.

E-mail: tolu.loto@gmail.com

Keywords: maize husk, corrosion management, pitting, aluminium, composite

OPEN ACCESS

RECEIVED
2 September 2022

REVISED
10 October 2022

ACCEPTED FOR PUBLICATION
21 October 2022

PUBLISHED
3 November 2022

Abstract

The effect of maize husk (MH) particulates on the corrosion resistance of 1070 aluminium alloy (AA70) matrix at 5% and 15% wt. content, and 150 μm and 300 μm particle size (AA70/MH composites) was studied in 3.5% NaCl, 0.0125 M H_2SO_4 and 3.5% NaCl/0.0125 M H_2SO_4 solutions. Potentiodynamic polarization technique, open circuit potential measurement, weight loss analysis, optical microscopy characterization, x-ray fluorescence and x-ray diffractometry were used for the investigation. Results show increase in MH %wt. content and particle size decreases the corrosion rate of AA70/MH composite. Data from potentiodynamic polarization and weight loss analysis shows AA70/MH composite at 15% wt. content and 300 μm particle size exhibited the lowest corrosion values of 0.135 mm y^{-1}, 0.156 mm y^{-1} and 1.445 mm y^{-1}, and −0.00043 mm y^{-1}, 0.001 04 mm y^{-1} and 0.00218 mm y^{-1} in 3.5% NaCl, 0.0125 M H_2SO_4 and 3.5% NaCl/0.0125 M H_2SO_4 solutions. Optical representative images of the composites showed the presence of micro-pits on samples from NaCl solution, macro-pits and extensive surface deterioration from H_2SO_4 solution, and combined localized and total surface deterioration from NaCl-H_2SO_4 solution. Weight loss plots showed oxide formation significantly influenced the corrosion behavior of the alloys with respect to time. Open circuit potential plots showed AA70/MH composite at 5% wt. content and 150 um particle size was the most electronegative with the highest thermodynamic tendency to corrosion. Significant X-ray diffraction peaks from AA70/MH composite at 15% wt. content and 300 μm particle size showed the presence of corrosion resistant phase compounds of Al_2O_3 and $Al(ZnS_2)$ before and after corrosion.

Introduction

The difficulty in identifying pure metallic materials that meets the service requirements of industry and engineering applications necessitates the addition of metallic and non-metallic reinforcements and elements to improve their properties for weight decrease, increased efficiency and high performance. The physical, mechanical, electrical, thermal, thermo-mechanical, tribological and wear resistance properties of metallic alloys continually undergo improvement and modifications to satisfy operational and in-service requirements of consumers and industries [1, 2]. Research into, and production of composites materials have been the major focus of attention in emerging materials industry for the production of products that combines excellent mechanical properties with corrosion resistance and aesthetic value [3]. Aluminium matrix composites are a class of lightweight aluminium alloys impregnated with specific materials responsible for the formation of complex intermetallic phases within the alloy matrix and heterogeneous microstructural properties [4]. The composite reinforcements could be in the form of continuous or discontinuous fibres, whisker or particulates in varying volume fractions integrated into a continuous phase. Research on aluminium matrix composites have proven beyond doubt the advantages of the composites over their base substrate metal [5]. The composites impart strength to the aluminium matrix that matches the strength of steel at half its weight. The resulting effect is the extensive application of aluminium matrix composites in the production of parts and components in agriculture,

aeronautical, bicycle, automobile, mining, construction and marine industries [6–8]. Various composites reinforcements have been tested and used in aluminium alloy matrix [9]. Silicon carbide (SiC) and aluminium oxide (Al_2O_3). enhances the tensile strength, compressive strength, wear resistance, hardness and density of aluminium alloy [10, 11]. Impregnation of boron carbide (B_4C) into the aluminium alloy matrix improves the hardness of the alloy [12]. Zirconium has been noted to increase the wear resistance of aluminium alloys [13]. Fly ash has also been used due to their economic value, availability and low density properties [14]. Other reinforcement such as rice husk, coconut husk, lignite ash has been used to achieve property requirements [15]. Research on graphene as a reinforcement material has been ongoing due to its higher dispersion and bonding properties with the matrix for application in automotive and aerospace industry [16–18]. Significant research on aluminium matrix composites has focused on their production and processing techniques, and their mechanical properties [19–23]. However, another major concern of reinforced matrix composites is the significant impact of the reinforcement on the corrosion rate of the matrix composites. Protective oxide film decreases with the corrosion rate in aluminum alloy-based composite [24]. The addition of reinforcement phase could cause discontinuities or flaws in the protective film. Composite reinforcements undergo electrochemical interactions with the matrix substrate, enhancing the microstructural deterioration of the composites [25–27]. Coupled with these galvanic reactions between the reinforcement and matrix also increase their rate of deterioration. This tends to be localized along the matrix interface leading to rapid penetration detrimental to structural stability of the composites in service. Localized attack on structural and compositional in-homogeneities can occur within the matrix leading to consequential failures. Corrosion resistance properties of aluminium matrix composites is a significant prerequisite for judging the performance and properties of the composites for structural applications [28]. Resistance of aluminium matrix composites to corrosion depends on its composite composition, manufacturing methods, dispersion of reinforcements in the continuous phase and environmental factors [29]. It must be noted that manufacturing processes enables uniform dispersion of reinforcement materials within the aluminium matrix invariably influencing the grain structure of the matrix composites [30–32]. Despite the shortcomings regarding the corrosion resistance of aluminium matrix composites, some investigations have shown that presence of some reinforcements in aluminium matrix do enhance the corrosion resistance of the matric composites. Obi *et al* studied the effect of fly ash reinforcement on the corrosion resistance of A535 aluminium alloy and its composites at 10 wt.% to 15 wt.% fly ash. Results show the general corrosion rate of the composite increased with increase in fly ash content while the critical pitting potential decreased with increasing fly ash content [33]. Corrosion behavior of the Al7075 composites prepared with carbon nanotubes as the potential reinforcements was studied. The composites were added to the base material in 2 wt.% to 6 wt.% in HCl solution. Results show decrease in corrosion rate with increase in carbon nano tube concentration [34]. The corrosion resistant properties of aluminium 6061 alloy reinforced with zircon particle composite, was studied in sodium hydroxide solution by open circuit potential methods. Results show potential decreases with respect to exposure time before attaining passivation [35]. Mamatha *et al* studied the corrosion resistance of aluminium 7075/ red mud metal matrix composites in neutral chloride solutions. Corrosion rate was observed to decrease with increase in the exposure time reinforcement content of the composites [36]. Narayanan *et al* evaluated the corrosion behaviour of nanographene oxide reinforced aluminium metal matrix composites. Results show corrosion rate decreased with increasing immersion time periods [37]. Mallireddy and Siva studied the corrosion resistance of aluminium matrix composite (7010—TiB) at 5–10 wt.% content. The matrix composite exhibited significant resistance to corrosion at 10% TiB shows [38]. Aluminum (Al6061) reinforced with ZrO_2 was investigated at 0% to 15 vol% of ZrO_2 for its corrosion resistance properties. Corrosion rate of substrate Al6061 was determined to be higher than its composite counterparts [39]. Shargh [40] studied the influence of post weld heat treatment on electrochemical and microstructural characteristics of explosive bonded interface of AA5083/ AA1050/SS 321 tubes at 350 and 450 °C. Results show variation in thickness and concentration of alloying elements in locally melting zone. Rate of corrosion and electrical charge transfer was observed to decrease. The corrosion resistance of aluminium/copper joint fabricated through explosive welding process was studied by Jandaghi *et al* [41]. Results show that the higher the stand-off distance the greater the increase in corrosion potential at the interface. Consequent upon the above and in contribution to research on the effect of reinforcements on the mechanical, thermal and corrosion resistance properties of aluminium composites, application of maize husk a sustainable materials of plant origin was studied as particle reinforcement on aluminium matrix for possible replacement of the conventional inorganic reinforcements.

Experimental methods

Materials and preparation

AA1070 aluminium metal (AA70) obtained from Aluminium Rolling Mills, at Ota town in Ogun State, Nigeria was analysed and determined to have the following (wt. %) composition presented in table 1. Maize husk (MH)

Table 1. Percentage nominal composition of AA70.

Element Symbol	Fe	Si	Mn	Cu	Zn	Ti	Mg	Pb	Sn	Al
% Composition	0.232	0.078	0.000	0.0006	0.0016	0.006	0.0027	0.0012	0.007	99.66

Table 2. Designation of AA70 with respect to MH particle size and wt.% content.

Specimens	Designation	MH Particle Size (μm)	MH wt.%
A	AA70	—	0
B	AA70/5%/150μm	150	5
C	AA70/5%/300μm	300	5
D	AA70/15%/150μm	150	15
E	AA70/15%/300μm	300	15

was obtained from the open market in Lagos state, Nigeria. It was dried for two weeks in open air and processed in line with the steps detailed in [39], which includes manual cleaning, drying, chopping, and milling to attain a powdery texture. The MH was subsequently dried in an oven before being milled and sieve analysis was performed to filter out the coarse grains and retained powder with particle sizes of 150 μm and 300 μm. The texture is important for homogeneity of the resulting MH composite with focus on the particle size, mix ratios, and particle behavior due to their influence on the synthesis of aluminum based composites. The stir casting method is the process route used in this research. An inclined furnace of 20kg capacity with a graphite crucible within was employed to melt AA70 for approximately 45 min at 660 °C. The temperature of the molten aluminium was observed with using K-type thermocouple. MH at particle sizes 150 μm and 300 μm, and at wt. % of 5% and 15% was added to the molten AA70 at vortex of 500 rpm (stirred mechanically) before being cast into prepared sand moulds and cooled for 24 h. The resulting AA70 composite (AA70/MH) at 5% and 15% MH wt. % content, and 150 μm and 300 μm MH particle size are of cylindrical dimension with diameter of 110 mm and height of 30 mm. The designation of AA70 composite with respect to MH particle size and wt.% content are shown in table 2. They were cut with power hacksaw and underwent metallographic preparation using abrasive emery papers (80, 320, 600, 800 and 1000 grit), washed with deionized water and acetone for subsequent electrochemical tests. Recrystallized NaCl obtained from Titan Biotech, India was formulated in percentage concentration of 3.5% electrolyte. Analar grade H_2SO_4 was formulated in molar concentration of 0.0125 M, and a third electrolyte consisting of the admixture of 3.5% NaCl and 0.0125 M of H_2SO_4 (3.5% NaCl/0.0125 M H_2SO_4) was also prepared.

Potentiodynamic polarization test

Potentiodynamic polarization was performed on AA70 and AA70/MH specimens with MH particle sizes of 150 μm and 300 μm at 5% and 15% wt.%. Pt counter electrode, Ag/AgCl reference electrodes and acrylic casted AA70 and AA70/MH working electrodes were placed within a transparent beaker filled with 200 ml of each electrolyte (3.5% NaCl, 0.0125 M H_2SO_4 and 0.0125 M H_2SO_4/3.5% NaCl). The electrodes were attached to Digi-Ivy 2311 potentiostat linked to a computer system. Polarization curves were plotted at sweep rate of 0.0015 V s^{-1} and set at potentials of −1.4 V to −0.55 V, −1.35 V to 0.08 V and −1.25 V to −0.60 V respectively for the NaCl, H_2SO_4 and NaCl-H_2SO_4 solutions. Corrosion current density, C_d (A cm^{-2}) and corrosion potential, C_p (V) values were obtained from the crosslink of the anodic-cathodic polarization curves produced by Tafel extrapolation. Corrosion rate, C_R (mm y^{-1}) and inhibition efficiency, η (%) were determined from the expression below;

$$C_R = \frac{0.00327 \times C_d \times E_q}{D} \quad (1)$$

D represents density in (g cm^{-3}); E_q indicates alloy equivalent weight (g). 0.00327 stands for corrosion rate constant.

Open circuit potential (OCP) measurement and optical microscopy characterization

OCP measurements were performed at step potential of 0.1 V s^{-1} for 2400 s in 3.5% NaCl, 0.0125 M H_2SO_4 and 0.0125 M H_2SO_4/3.5% NaCl solution with the same electrode configuration as the potentiodynamic polarization test. Optical images of AA70 and AA70/MH (at 150 μm and 300 μm particle size, and 5% and 15% wt.% content) surface morphologies were obtained and analysed with three different microscopes (Omax trinocular metallurgical microscope, HD G1200 Digital Microscope and Professional HD USB Microscope).

Weight loss analysis

Weight of the specimens were recorded at 24 h interval with Ohaus PA114 measuring device with resolution of 0.0001g, maximum capacity is 110g, repeatability is 0.1 mg and linearity is $\pm$0.2 mg. Weight loss was determined from the subtraction between the initial weight of AA70 and AA70/MH (maintained for 264 h) and subsequent weight measured at 24 h interval for a total of 240 h. Corrosion rate of AA70 and AA70/MH was determined from the equation below;

$$C_R = \left[\frac{87.6W}{\rho AT}\right] \tag{2}$$

W denotes weight loss (g), ρ denotes density (g cm^{-2}), A denotes area (cm^2), and T symbolizes time of exposure (h). Inhibition efficiency (η) was enumerated from the following equation;

$$\eta = \left[\frac{\omega_1 - \omega_2}{\omega_1}\right] \times 100 \tag{3}$$

ω_1 denotes weight loss of AA70 and AA70/MH from the acid solution without the distillates while ω_2 denotes weight loss of AA70 and AA70/MH at precise extract concentration.

X-ray diffractometry

X-ray diffraction plots and pattern list of the phase compounds, precipitates and metallic complexes on AA70 and AA70/MH composites (samples A, B and E) surface were produced. The data was obtained after analysis with Rigaku D/Max-lllC x-ray diffractometer at scanning rate of 2° min^{-1} in the 10 to 140° at room temperature with a CuKa radiation set at 40 kV and 20 mA in 2θ. The diffraction data (relative intensity) obtained was matched with the standard data of minerals from the mineral powder diffraction file, ICDD which contained and includes the standard data of more than 3000 minerals.

Results and discussion

Potentiodynamic polarization studies and optical microscopy characterization

The potentiodynamic polarization plots for AA70 and AA70/MH composites (samples A, B, C, D and E) from 3.5% NaCl, 0.0125 M H_2SO_4 and 3.5% NaCl/0.0125 M H_2SO_4 solution representing data from accelerated corrosion test are shown in figures 1(a)–1(c). Figures 2(a) and (b) shows the surface morphology of representative AA70 sample after metallographic test and after etching in in 2M $FeCl_3$ solution. Figures 2(c) to (e) shows the representative image of the samples after corrosion in 3.5% NaCl, 0.0125 M H_2SO_4 and 3.5% NaCl/0.0125 M H_2SO_4 solutions. The plots in figures 1(a) and (c) displays extended cathodic polarization slope compared to their anodic counterpart for all the samples signifying resistance to cathodic polarization of AA70 and AA70/MH composites. The similar configuration of the plots in figure 1(a) shows the cathodic behavior of the samples are under activation control in the presence of Cl^- anions compared to figure 1(c) where the reduction reaction under the influence of Cl^-/SO_4^{2-} anions tends to vary widely with respect to MH wt.% content and particle size. The general plots configuration shows the presence of Cl^-/SO_4^{2-} anions shifts the corrosion potential of the plots to anodic values signifying higher oxidation of the samples. The plot in figure 1(b) exhibits corrosion potential at relatively higher values compared to the plots in figures 1(a) and (c) which signifies a higher influence of SO_4^{2-} anions on the redox electrochemical processes occurring on the samples. This is evidenced by the higher cathodic-anodic Tafel slopes on the plots. Shift in corrosion potential occurred on the polarization plot in figures 1(b). This shift is in proportion to the variation in MH %wt. content and particle size due to cathodic polarization responsible for the weakening of the inert oxide. This causes selective dissolution on the composite surface [42, 43].

Figure 1(c) also exhibits significantly higher anodic slope confirming the dominant effect of oxidation half-cell reactions. However, this observation contrasts the anodic plot configuration in figure 1(a) where visible but limited passivation of the oxidation reaction occurred. This is also evident on the slopes of the anodic polarization plots where irregularities in the plots occurred despite passivation tendencies due to active-passive behaviour of the protective oxide (Al_2O_3) formed on the samples in the presence of Cl^- anions. Hence, there is

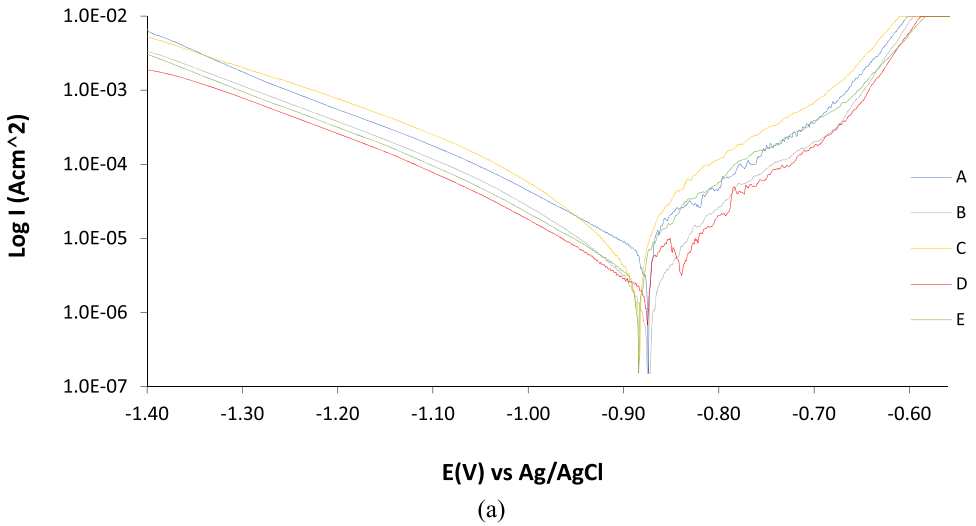

(a)

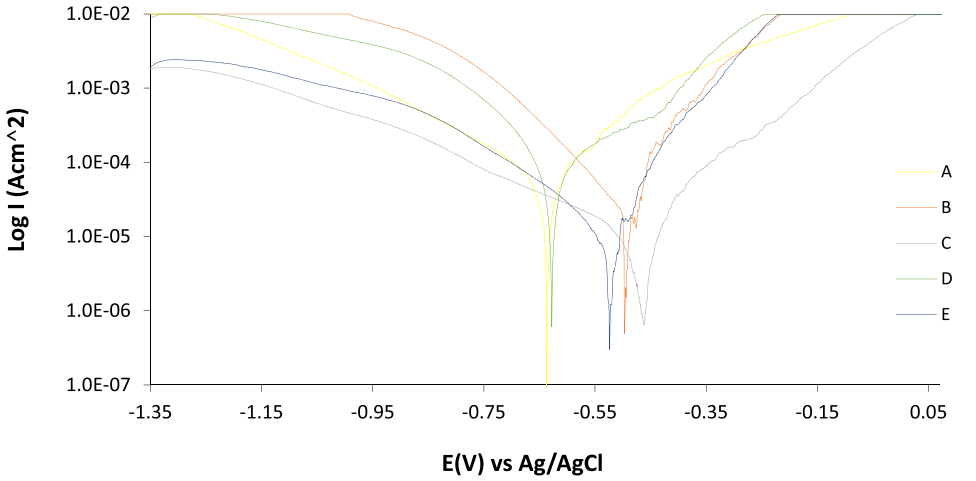

(b)

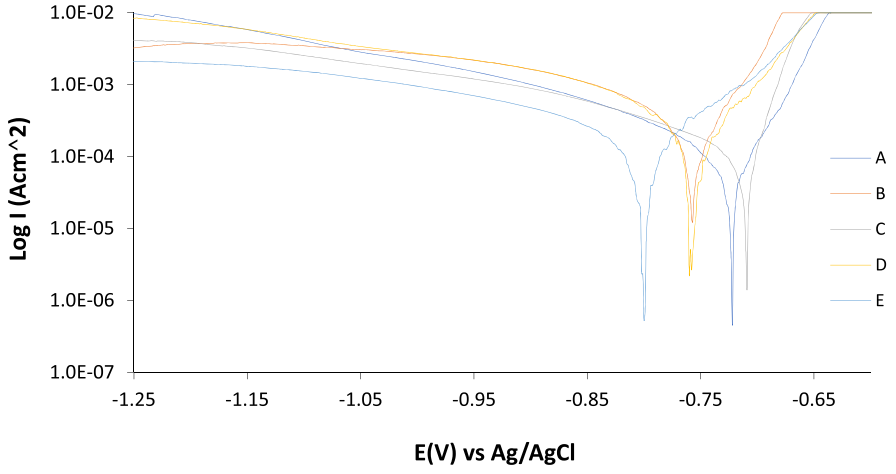

(c)

Figure 1. Potentiodynamic polarization plots for AA70 and AA70/MH composites (samples A to E) in (a) 3.5% NaCl, (b) 0.0125M H_2SO_4 and (c) 3.5% NaCl/0.0125M H_2SO_4 solution.

the possibility of extensive localized degradation by Cl^- ions due to galvanic effect between continuous microstructure of Al substrate metal, intermetallic phases, precipitates, impurities and discontinuities caused by the presence of MH [44, 45]. The discontinuity is responsible for the evolution of transient $Al_2O_3.3H_2O$ on the composite surface, resulting from the transformation of $Al(OH)_3$ in the electrolyte [46]. The corrosion rate and other electrochemical data for the samples in NaCl, H_2SO_4 and NaCl-H_2SO_4 solution are shown in table 3. Observation of the table shows samples in NaCl-H_2SO_4 solution exhibited the highest corrosion rate values

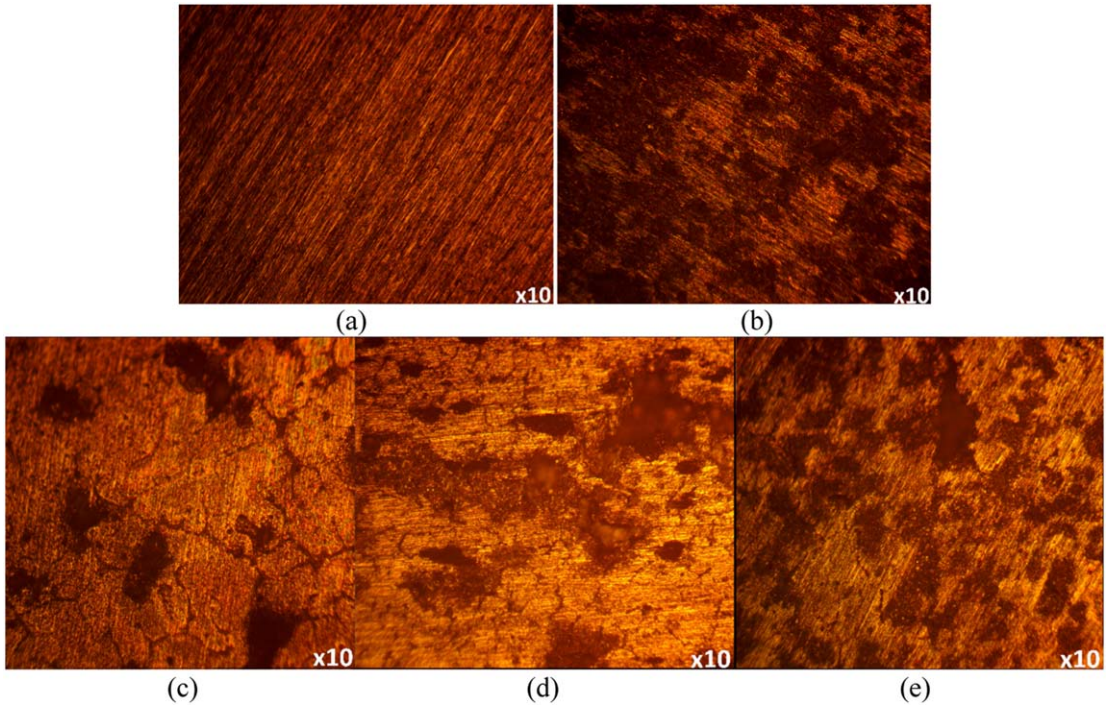

Figure 2. Optical representative images of samples A to E at mag. x10 (a) image before sample preparation, (b) image after etching in 2M $FeCl_3$ solution, (c) from 3.5% NaCl solution, (d) from 0.00125 M H_2SO_4 and (e) from 3.5% NaCl/0.00125 M H_2SO_4 solution.

Table 3. Potentiodynamic polarization data for AA70 and AA70/MH composites (samples A to E) in 3.5% NaCl, 0.0125M H_2SO_4 and 3.5% NaCl/ 0.0125M H_2SO_4 solution.

MH Content and Particle Size	Corrosion Rate (mm y^{-1})	Corrosion Current (A)	Corrosion Current Density (A cm^{-2})	Corrosion Potential (V)	Polarization Resistance, R_p (Ω)	Cathodic Tafel Slope, B_c (V dec^{-1})	Anodic Tafel Slope, B_a (V dec^{-1})
3.5% NaCl Solution							
A	0.276	2.55E-05	2.55E-05	−0.874	1009.00	−7.057	2.55E-05
B	0.321	2.96E-05	2.96E-05	−0.872	878.00	−9.084	4.96E-06
C	0.183	1.69E-05	1.69E-05	−0.883	1524.00	−9.734	1.69E-05
D	0.149	1.37E-05	1.37E-05	−0.875	1876.00	−7.762	1.37E-05
E	0.135	1.25E-05	1.25E-05	−0.884	2057.00	−7.027	1.25E-05
0.0125M H_2SO_4 Solution							
A	0.571	5.26E-05	5.26E-05	−0.637	488.10	−5.155	4.557
B	0.609	5.61E-05	5.61E-05	−0.497	458.00	−7.850	12.970
C	0.230	2.12E-05	2.12E-05	−0.463	901.00	−4.964	9.823
D	0.180	1.66E-05	1.66E-05	−0.562	1214.00	−5.636	7.717
E	0.156	1.44E-05	1.44E-05	−0.524	1784.00	−6.809	14.040
3.5% NaCl/0.0125M H_2SO_4 Solution							
A	3.075	2.84E-04	2.84E-04	−0.722	87.00	−6.649	27.660
B	3.534	3.26E-04	3.26E-04	−0.757	78.87	−5.829	21.510
C	2.901	2.67E-04	2.67E-04	−0.709	96.09	−5.431	20.437
D	2.856	2.63E-04	2.63E-04	−0.760	97.60	−5.748	19.860
E	1.445	1.33E-04	1.33E-04	−8.000	193.00	−5.019	10.430

Table 4. Corrosion rate results for AA70 and AA70/MH composites (sample A to E) from 3.5% NaCl, 0.0125M H_2SO_4 and 3.5% NaCl/0.0125M H_2SO_4 solutions at 264 h of exposure.

AA70/MH Composite Samples	3.5% NaCl Solution	0.0125M H_2SO_4 Solution	3.5% NaCl/0.0125M H_2SO_4 Solution
A	−0.00040	0.00114	0.00260
B	−0.00007	0.00138	0.00309
C	−0.00037	0.00079	0.00237
D	−0.00028	0.00104	0.00190
E	−0.00043	0.00104	0.00218

compared to the samples in NaCl and H_2SO_4 solution. The high corrosion rate value is closely aligned with increase in corrosion current density as a result of the collapse of the inert oxide formed and the localized degradation [47, 48].

The oxidation of AA70 and AA70/MH composites (samples A to E) as shown in the anodic portion of the polarization plots in figures 1(a) to (c) is due to the acidification of the samples surface, resulting from the competitive adsorption of Cl^- anions and O_2, SO_4^{2-} ions and O_2, and Cl^-/SO_4^{2-} anions and O_2 leading to the formation of complexes that further aggravates the corrosion process. However, this phenomenon is quite limited but inevitable in figure 1(a) due to the localized deteriorating action of Cl^- anions. This assertion is proven on the image in figure 2(c) where micro-pits and corrosion along the grain boundaries are visible. The anodic-cathodic Tafel slope values in figure 1(b) counterbalance each other compared to the plots in figures 1(a) and (c), signifying destruction of the protective oxide on AA70 and its composites. The image in figure 2(d) shows enlarged corrosion pits and degradation over the sample surface. Within NaCl-H_2SO_4 solution, sample B (AA70/MH at 5% wt./150 μm) exhibited the highest corrosion rate at 3.075 mm y^{-1} corresponding to corrosion current density of 2.84E-04 A cm^{-2} and polarization resistance of 88 Ω. The optical image in figure 2(e) shows higher degree of surface degradation compared to figures 2(c) and (d). The combined action of Cl^- and SO_4^{2-} anions completely destroyed the protective oxide exposing the substrate alloy and composite fractions to corrosion. Beyond sample B, corrosion rate decreases progressively to 1.445 mm/y for sample E. Samples in NaCl solution exhibited the lowest corrosion rate values. At sample A corrosion rate is 0.276 mm/y. Corrosion rate increased to 0.321 mm/y for sample B. However, beyond sample B corrosion rate decreased similarly to the trend in NaCl-H_2SO_4 solution to 0.135 mm/y for sample E. Generally, sample B exhibited the highest corrosion rate in all the solutions studied. This shows AA70/MH composite at MH 5% wt. content and 150 μm particle size is the most vulnerable to accelerated corrosion. The higher the MH % wt. content and particle size, the lower the corrosion rate of the Al composite. MH reinforcement at 5% wt. content and 150 μm particle size (sample B) causes inhomogeneity's on the Al composite surface resulting in penetration by the corrosive anions through the discontinuity on the inert protective oxide [49]. Previous research has reported on decrease in corrosion rate with increase in reinforcement %wt. content and particle size. probably due to improved interfacial bonding between the MH particles, thus hindering diffusion of corrosive anions [50, 51].

Weight loss and optical macroscopy analysis

Data on corrosion rate results for samples A to E from weight loss analysis in 3.5% NaCl, 0.0125M H_2SO_4 and 3.5% NaCl/0.0125M H_2SO_4 solutions at 264 h of exposure are shown in table 4. Figures 3(a) to (c) shows the corresponding plots of corrosion rates versus exposure time throughout the exposure hours for the samples from the solutions earlier mentioned. Optical macroscopic images (mag. x5) of samples A to E are shown from figures 4(a) to (d). Figure 4(a) shows the representative etched sample image (mag. x5) before corrosion. The microstructural features are clearly visible. Figures 4(b)–(d) shows the representative images (mag. x5) of the samples from 3.5% NaCl, 0.0125M H_2SO_4 and 3.5% NaCl/0.0125M H_2SO_4 solutions. Figures 5(a) to (c) shows the shows the corresponding representative images at mag. x10 of the samples from 3.5% NaCl, 0.0125M H_2SO_4 and 3.5% NaCl/0.0125M H_2SO_4 solutions. Table 4 shows AA70 and AA70/MH composites (sample A to E) generally exhibited decrease in corrosion rate at 264 h of exposure in NaCl solution due to formation and growth of the inert oxide on the surface of the samples and the formation of complexes with adsorbed Cl^- anions. However, it is observed that sample B exhibited the lowest amount of oxide formed on its surface with final corrosion rate of −0.00007 mm y^{-1} while sample E exhibited the highest amount of oxide complexes formed on its surface. Sample B also exhibited the highest corrosion rate in H_2SO_4 and NaCl/H_2SO_4 solution. Beyond sample B, corrosion rate decreased in the presence of SO_4^{2-} and Cl^-/SO_4^{2-} anions. The plot configurations in figures 3(a) and (b) shows significant increase in corrosion rate values generally for the first 72 h and 96 h beyond which relative stability was attained. This observation however does not include the plot for sample B where in figure 3(a) it was generally constant at relatively higher corrosion rate values while in figure 3(b) its corrosion rate continues to increase till 264 h. The optical image in figure 4(b) relating to the representative image from NaCl

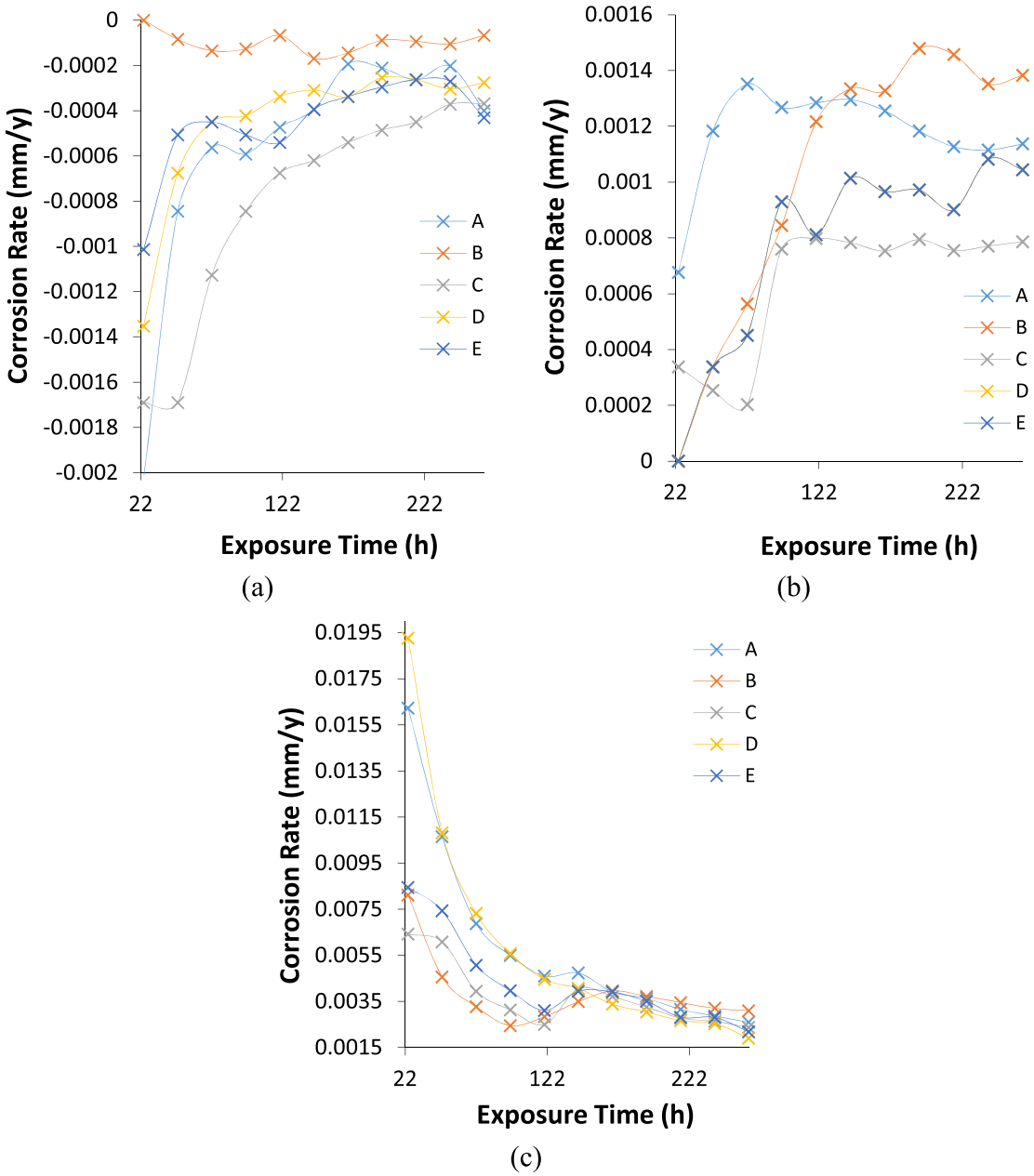

Figure 3. Plot of corrosion rate results for AA70 and AA70/MH composites (sample A to E) from 3.5% NaCl, 0.0125M H_2SO_4 and 3.5% NaCl/0.0125M H_2SO_4 solutions from 24h to 264 h of exposure.

solution showed dentritic microstructures with white spots caused by entrapment of moisture on the sample surface forming Al_2O_3. This proves the partial formation of protective oxide on the surface in addition to corrosion along the grain boundaries of the Al-composite surface. The corresponding higher resolution of the image in figure 5(a) shows corrosion along the grain boundaries and formation of micro-pits. The optical image in figure 4(c) relating to corrosion from H_2SO_4 solution reveals the absence of the whitish protective oxide. Secondly, the dentritic microstructure is significantly more visible due to greater deterioration of surface properties of the composite along the grain boundaries. The corresponding higher resolution of the image in figure 5(b) shows the formation of macro-pits [larger pits than the ones in figure 5(a) from NaCl solution] and great degree of degradation. Figure 4(c) shows quite the opposite with the corrosion rate of the samples decreasing before attaining relative stability at around 96 h to 120 h. This observation is due competitive adsorption of the corrosive species which invariably formed pseudo passive state on the composites and thus decreasing the corrosion rate of the composite. The image in figure 4(d) attest to this assertion as its morphology shows the combined deteriorating action of Cl^-/SO_4^{2-} anions on the composite surface. The corresponding higher resolution of this image in figure 5(c) exposes the extent of deterioration which significantly exceeds the degree of deterioration of the composite from NaCl and H_2SO_4 solution. Nevertheless, sample B exhibited the highest corrosion value at 264 h of exposure.

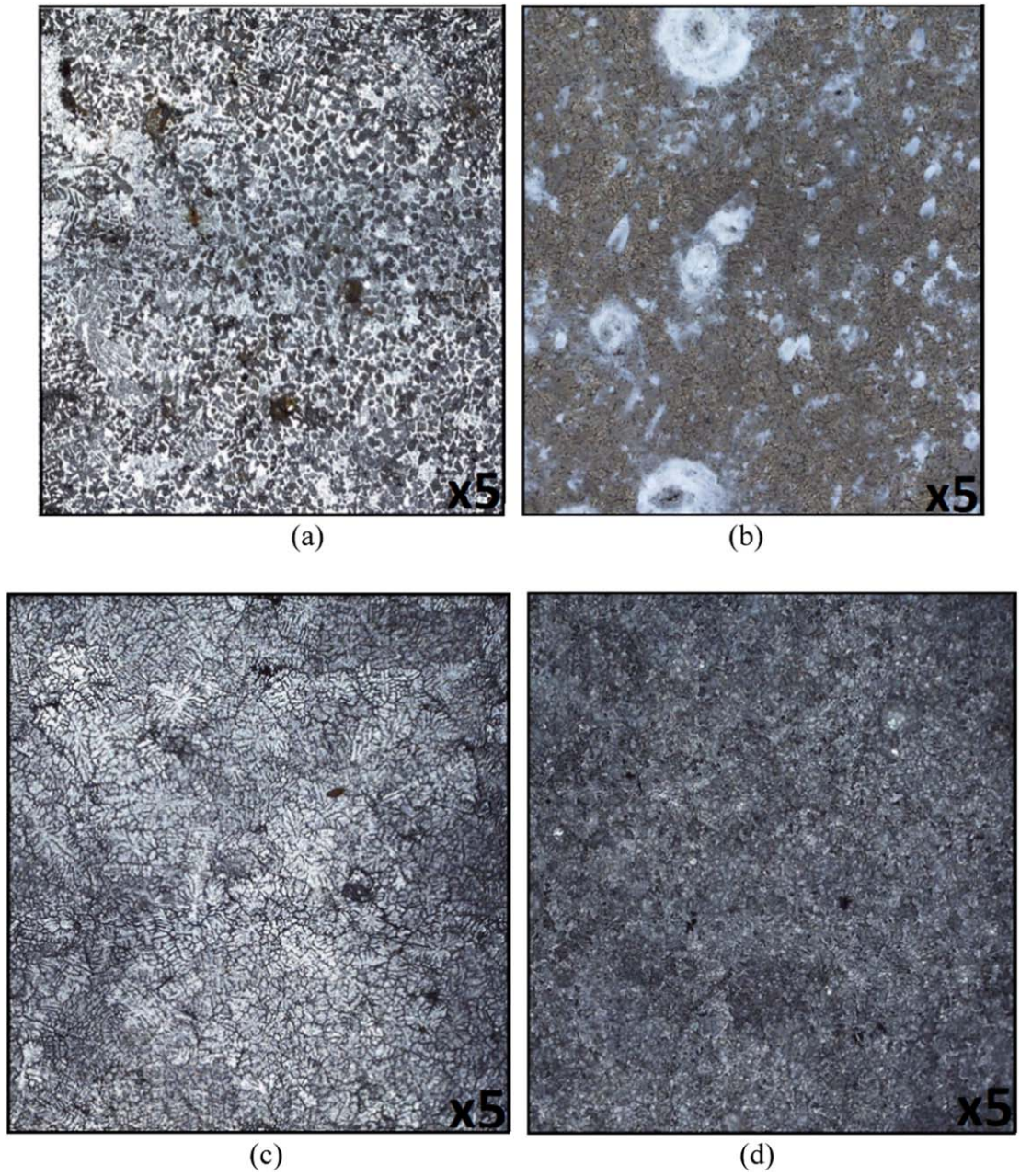

Figure 4. Optical representative images of AA70 and AA70/MH composites (sample A to E) at mag. x5. (a) etched surface before corrosion test, (b) corroded surface from 3.5% NaCl solution, (c) corroded surface from 0.0125 M H_2SO_4 solution and (d) corroded surface from 3.5% NaCl/0.0125 M H_2SO_4 solution.

X-ray fluorescence analysis

Tables 5 and 6 shows the normalized x-ray fluorescence data for AA70 and AA70/MH composite samples (sample A, sample B and sample E) before and after corrosion in 3.5% NaCl/0.0125M H_2SO_4 solution. The elements/compounds identified are shown in the tables consisting of TiO_2, CaO, Na_2O, SiO_2, Al_2O_3 and MgO. The two major observations from the tables are (i) the % composition of the elements (excluding Al_2O_3) for the samples studied decreased significantly after corrosion. This is due to oxidation of the composites alloy in the presence of debilitating action of combined Cl^- and SO_4^{2-} anions in the acid-chloride solution. (ii) Al_2O_3 the principal compound responsible for corrosion increased in concentration due to the adsorption of O_2 atoms in the aqueous media despite corrosion of the composite. Sample A being the monolithin Al alloy exhibited the highest % concentration of Al_2O_3. However, after corrosion sample E which exhibited the least corrosion rate from weight loss and potentiodynamic polarization exhibited the highest concentration of Al_2O_3, representing a 59.87% increase in Al_2O_3 formation on the composite and aiding in its corrosion resistance. A significant decrease in SiO_2 was also observed. SiO_2 is a major component of the corrosion resistance properties of Al composite alloys with sample B exhibiting the highest value after corrosion compared to sample A before corrosion.

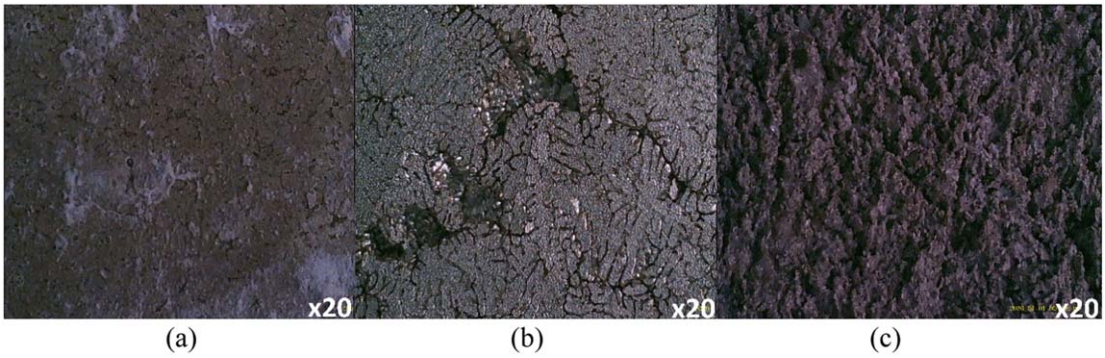

Figure 5. Optical representative images of AA70 and AA70/MH composites (sample A to E) at mag. x20 (a) corroded surface from 3.5% NaCl solution, (b) corroded surface from 0.0125 M H_2SO_4 solution and (c) corroded surface from 3.5% NaCl/0.0125 M H_2SO_4 solution.

Table 5. X-ray fluorescence data for sample A, Sample B and Sample E before corrosion from 3.5% NaCl/0.0125 M H_2SO_4 solution.

Specimens	Elements (%)					
	TiO_2	CaO	Na_2O	SiO_2	Al_2O_3	MgO
Sample A (Before Corrosion)	0.21	2.12	1.08	49.38	46.85	0.36
Sample B (Before Corrosion)	0.23	2.50	1.40	61.59	33.83	0.44
Sample E (Before Corrosion)	0.23	2.78	1.67	71.34	23.46	0.52

Table 6. X-ray fluorescence data for sample A, Sample B and Sample E after corrosion from 3.5% NaCl/0.0125 M H_2SO_4 solution.

Specimens	Elements (%)					
	TiO_2	CaO	Na_2O	SiO_2	Al_2O_3	MgO
Sample A (After Corrosion)	0.14	1.12	0.61	23.50	74.45	0.19
Sample B (After Corrosion)	0.16	1.40	0.82	31.75	65.63	0.25
Sample E (After Corrosion)	0.15	1.21	0.69	26.70	71.05	0.21

Open circuit potential measurement

The open circuit potential plots for AA70 and AA70/MH composites (samples A-E) from 3.5% NaCl, 0.0125 M H_2SO_4 and 3.5% NaCl/0.0125 M H_2SO_4 solution are shown in from figures 6(a) to (b). Comparison of the plots in figures 6(a) and (b) shows the significant variation in the starting potential of the plots. Corrosion potential of the plots in figure 6(a) initiated at values between −0.800 V and −0.757 V. Significant potential transients are visible on the plots due to the electrochemical action of Cl^- anions on AA70 and AA70/MH composite surfaces. The transients arise as the inert protective oxide on AA70 undergoes active-passive transition where the anions compete with O_2 for adsorption unto the surface. The transients are more visible on the plot for sample B which invariably had the highest corrosion rate from polarization test. There is the possibility of galvanic action which also contributes to the transients on the plots. The plots for sample D and E exhibited the relatively minimum potential transient. These samples (AA70/MH15%/150um and AA70/MH15%/300um) shows MH at higher %wt. and particle size significantly improves the corrosion resistance properties of the composite. Nevertheless, the plots generally showed thermodynamic stability in the presence of Cl^- anions. At 2400s, the plots culminated at potentials between −0.679 V and −0.740 V.

Comparing the plot configuration in figures 6(a) to (b), it is visible that the plot configuration shows significantly less potential transients compared to the plots in figure 6(a). This shows nature of anion contents significantly impacts the electrochemical behavior of the composite. Firstly, the plots occurred at significantly more electropositive corrosion potentials between −0.348 V and −0.542 V. This signifies lower tendency to electrochemical activity in the presence of SO_4^{2-} anions compared to Cl^- anions. Secondly, the potential transients in figure 6(b) fizzled out at around 700s, before which potential transients were significant and thirdly, the corrosion potential plots shifted from electropositive values to electronegative values before attaining thermodynamic stability at varying potentials and exposure time. The reason for the high potential transients in

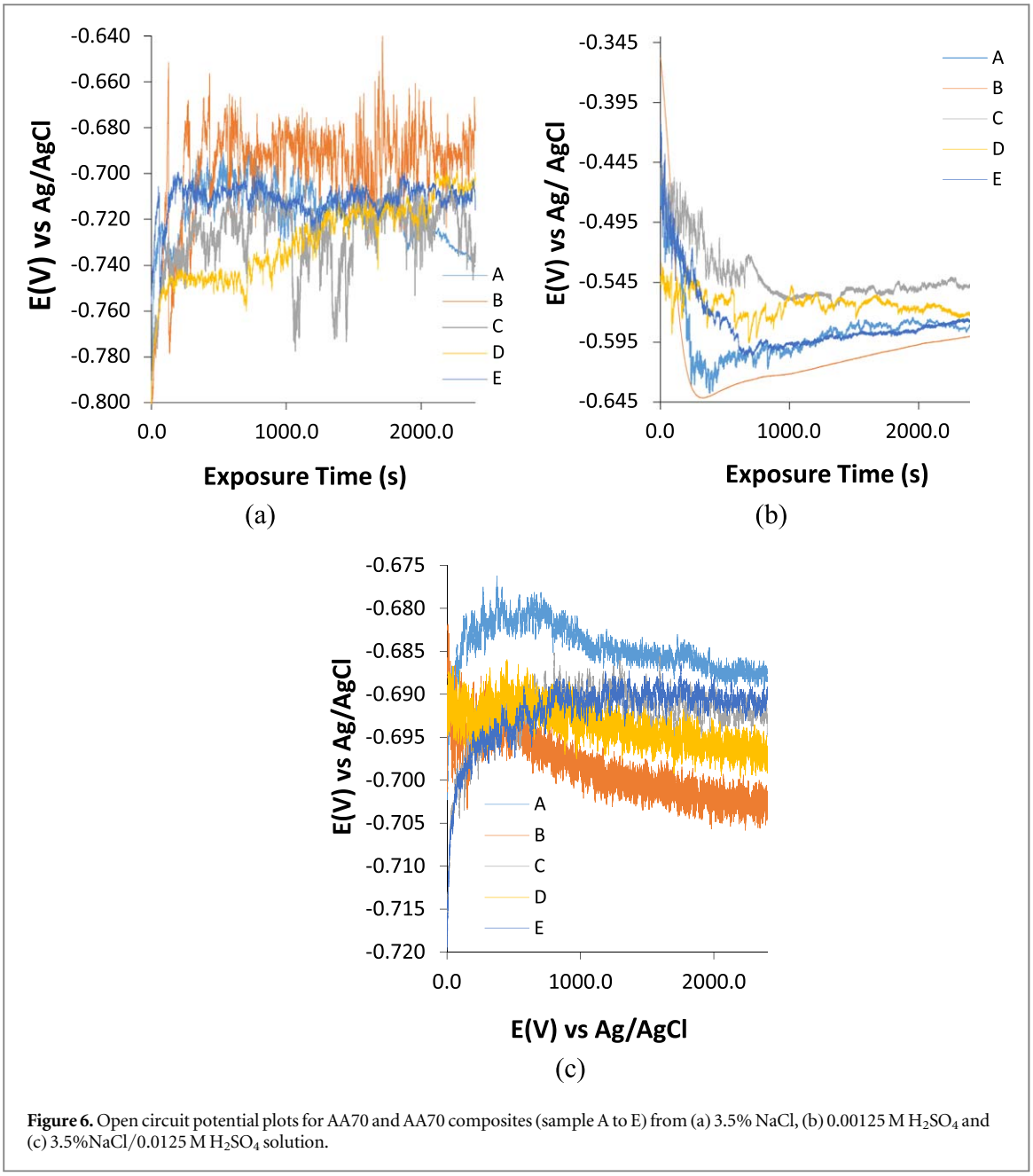

Figure 6. Open circuit potential plots for AA70 and AA70 composites (sample A to E) from (a) 3.5% NaCl, (b) 0.00125 M H_2SO_4 and (c) 3.5%NaCl/0.0125 M H_2SO_4 solution.

figure 6(a) compared to figure 6(b) is due to relatively small size of Cl^- anion and high reactivity compared to SO_4^{2-} anion which enables penetration through the discontinuities on the composite surface. It must be noted that sample B did not display any potential transient if figure 6(b) but exhibited the most electronegative plot i.e. higher corrosion tendency with final corrosion potential of −0.580 V at 2400s. There is the possibility of destruction of the protective oxide considering the sample exhibited the highest corrosion rate result from polarization test. The plot in figure 6(c) significantly differs from the plots in figures 6(a) and (b). Significant potential transients are visible on the plots in figure 6(a) due to the combined action of Cl^- and SO_4^{2-} anions responsible for penetration of the protection and destruction of the protective film. Secondly, competitive adsorption also influenced the electrochemical properties of the composite surface. The plots initiated at potentials between −0.694 V and −0.720 V, and culminated at potentials between −0.688 V and −0.703 V. The plot for sample B in figure 6(c) was the most electronegative at 2400s of exposure while its potential transients appeared denser.

X-ray diffractometry

X-ray diffraction analysis was performed on AA70 and AA70/MH composite samples (sample A, sample B and sample E) before and after corrosion test in 3.5% NaCl/0.0125 M H_2SO_4 solution. Figures 7(a) and (b) shows the diffraction plots for sample A before and after corrosion. Figures 8(a) and (b) shows the diffraction

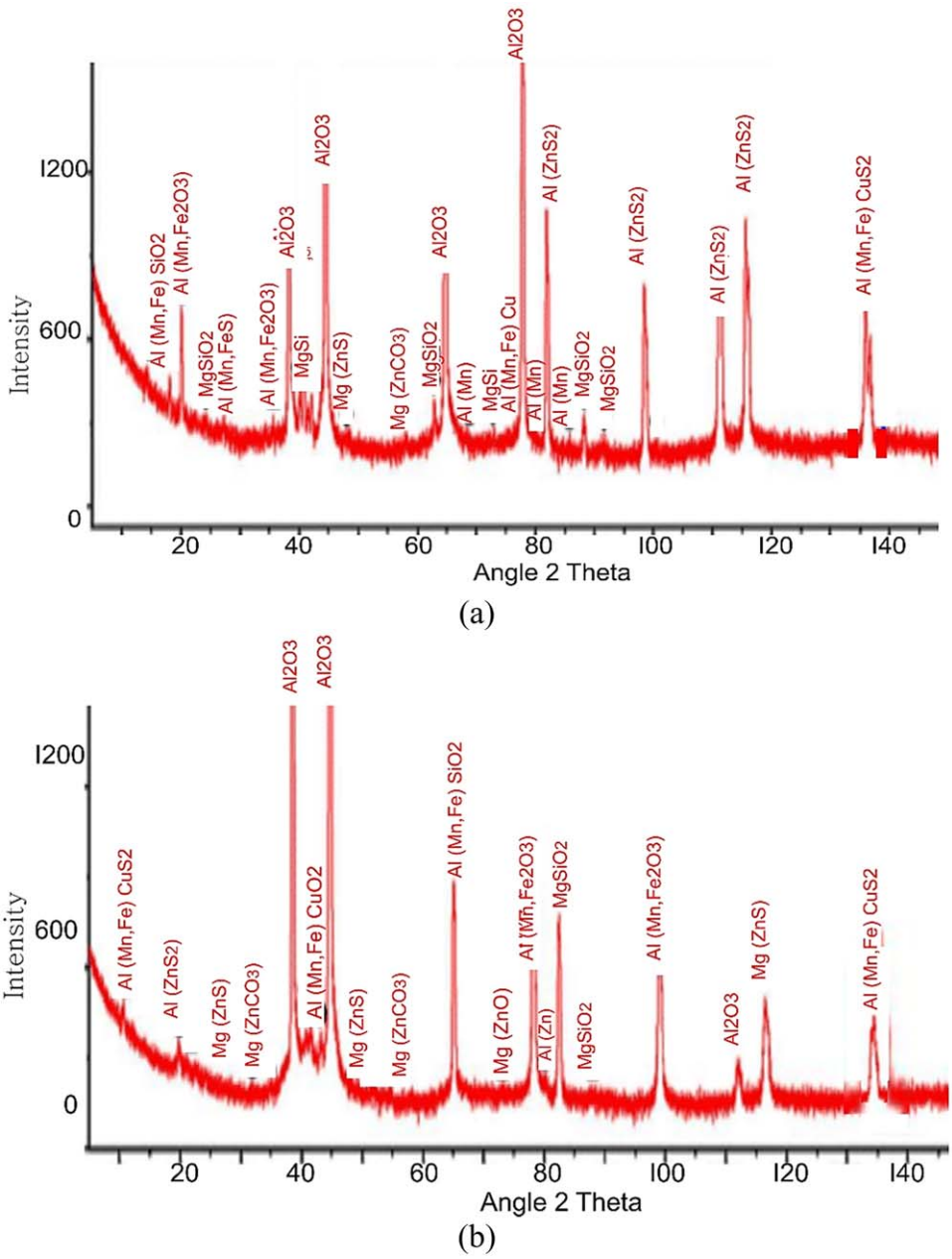

Figure 7. Representative XRD Phase identification plots for AA70 alloy (sample A), (a) before corrosion and (b) after corrosion in 3.5% NaCl/0.0125 M H_2SO_4 solution.

plots for sample B before and after corrosion while figures 9(a) and (b) shows the diffraction plots for sample E before and after corrosion. The diffraction peaks for sample A before corrosion (figure7(a)) at 2θ are 18.524, 19.580, 20.280, 22.301, 23.291, 35.185, 36.204, 37.302, 41.402, 43.101, 58.390, 62.407, 63.181, 64.203, 65.204, 78.196, 79.234, 80.282, 82.308, 83.302, 84.138, 100.300, 110.343, 115.214 and 138.454. The corresponding diffraction peaks for the sample after corrosion (figure7(b)) are 18.524, 19.580, 20.280, 22.301, 23.291, 35.185, 36.204, 37.302, 41.402, 43.101, 58.390, 62.407, 63.181, 64.203, 65.204, 78.196, 79.234, 80.282, 82.308, 83.302, 84.138, 100.300, 110.343, 115.214 and 138.454. The dominant diffraction peaks in figure 7(a) are Al_2O_3 and $Al(ZnS_2)$ at peak intensity values such as 480, 600, 400 and 300. Al_2O_3 is responsible for the passivation of Al alloys while insoluble $Al(ZnS_2)$ provides pseudo protection. After corrosion, most of the passive film (Al_2O_3) has been destroyed as shown in figure 7(b) with the remaining Al_2O_3 being product of repassivation after corrosion test from the aqueous media. The diffraction peaks in figure 7(b) shows the presence of other phase which are products of precipitation, chemical transformation and exposure from destruction of the passive film.

Observation of figures 8(a) and (b) shows significant variation in the phase compounds formed between them, and the phase compounds formed in figures 7(a) and (b). The dominant phase in figure 8(a) occurred at $2\theta = 20.590, 36.564, 41.652, 43.301, 63.201, 78.326, 80.282, 100.300$ and 115.214 which produced dominant

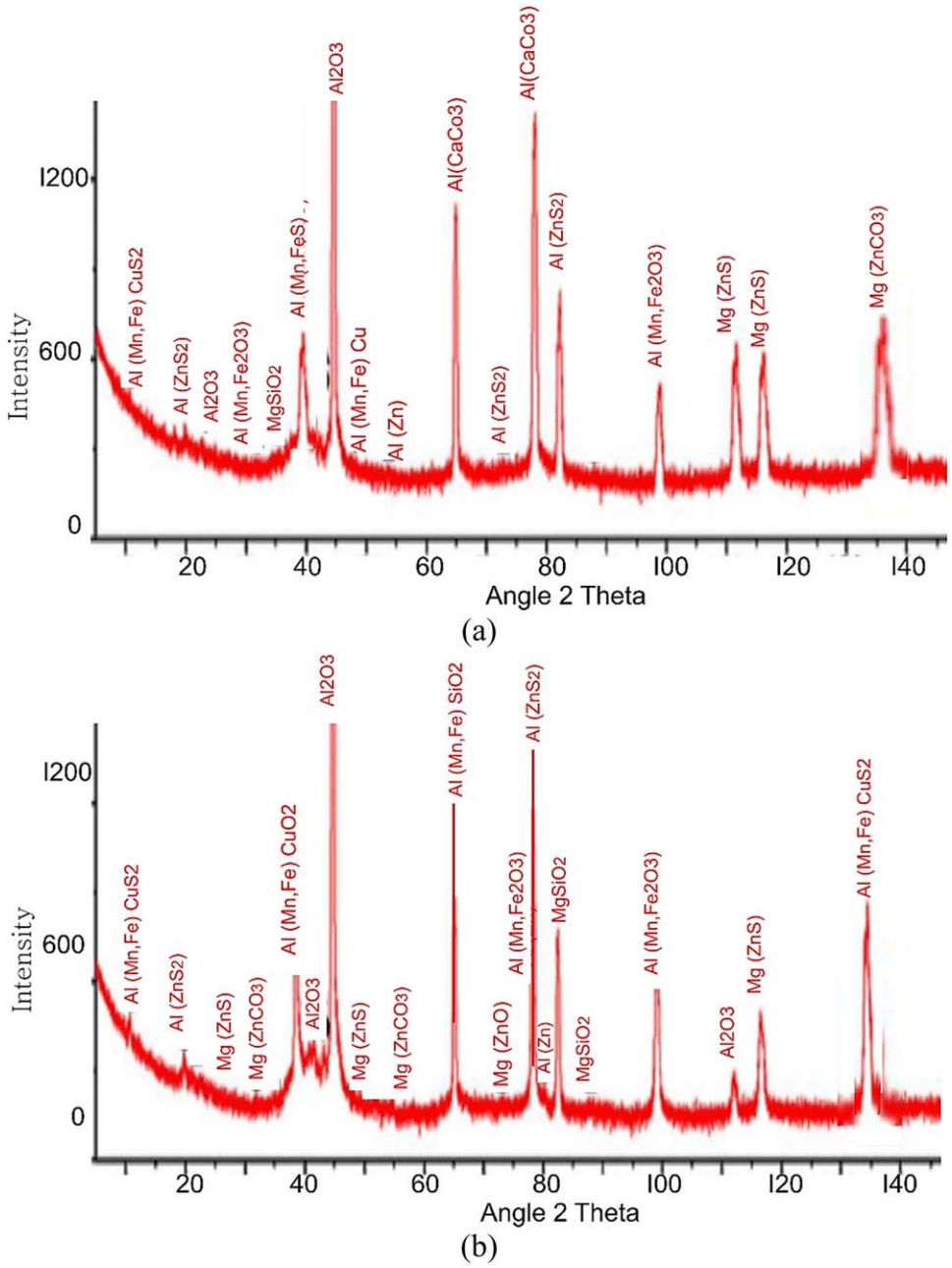

Figure 8. Representative XRD Phase identification plots for AA70/MH composite (sample B), (a) before corrosion and (b) after corrosion in 3.5% NaCl/0.0125 M H_2SO_4 solution.

peak intensities of 770, 800, 1300, 1300, 1000, 1300, 800, 680 and 800. The dominant phases are Al_2O_3, $Al(CaCO_3)$, $Al(ZnS_2)$ and $Mg(ZnCO_3)$ due to alteration of the metallurgical structure and microstructural properties of AA70 Al with 5% MH at 150 μm particle size. However, after corrosion the dominant phases occurred at $2\theta = 20.590, 36.564, 41.652, 43.301, 63.201, 78.326, 80.282$ and 115.214 corresponding to intensities of 770, 800, 1300, 1300, 1000, 1300, 800 and 800. These intensity values indicate dominant phases such as $Al(Mn, Fe)SiO_2$, $MgSiO_2$, $Al(Mn, Fe)CuS_2$, $Mn(Fe_2O_3)$. These phases differ from the phases in figure 7(b). The phases in figure 9(a) is dominated by Al_2O3 and $Al(ZnS_2)$. These compounds are significantly responsible for passivation of Sample E (AA70 Al at 15% MH wt. content and 300 μm particle size) as indicated by sample E exhibiting the highest corrosion rate. The passivation of the composite is influenced by the %wt. content and particle size of MH in sample E. The phase in sample E occurred at $2\theta = 20.280, 36.204, 37.302, 41.402, 63.181, 78.196, 80.282$ and 115.214 corresponding to peak intensities of 770, 800, 750, 1300, 700, 1300, 800 and 800. After corrosion, the remaining dominant phase is $Al(ZnS_2)$ an insoluble precipitate which occurred at $2\theta = 40.860$ and 62.618 corresponding to intensities of 1400 and 1300. The insoluble precipitate provides insoluble pseudo protection of the composite surface thus limiting the redox electrochemical processes responsible for corrosion.

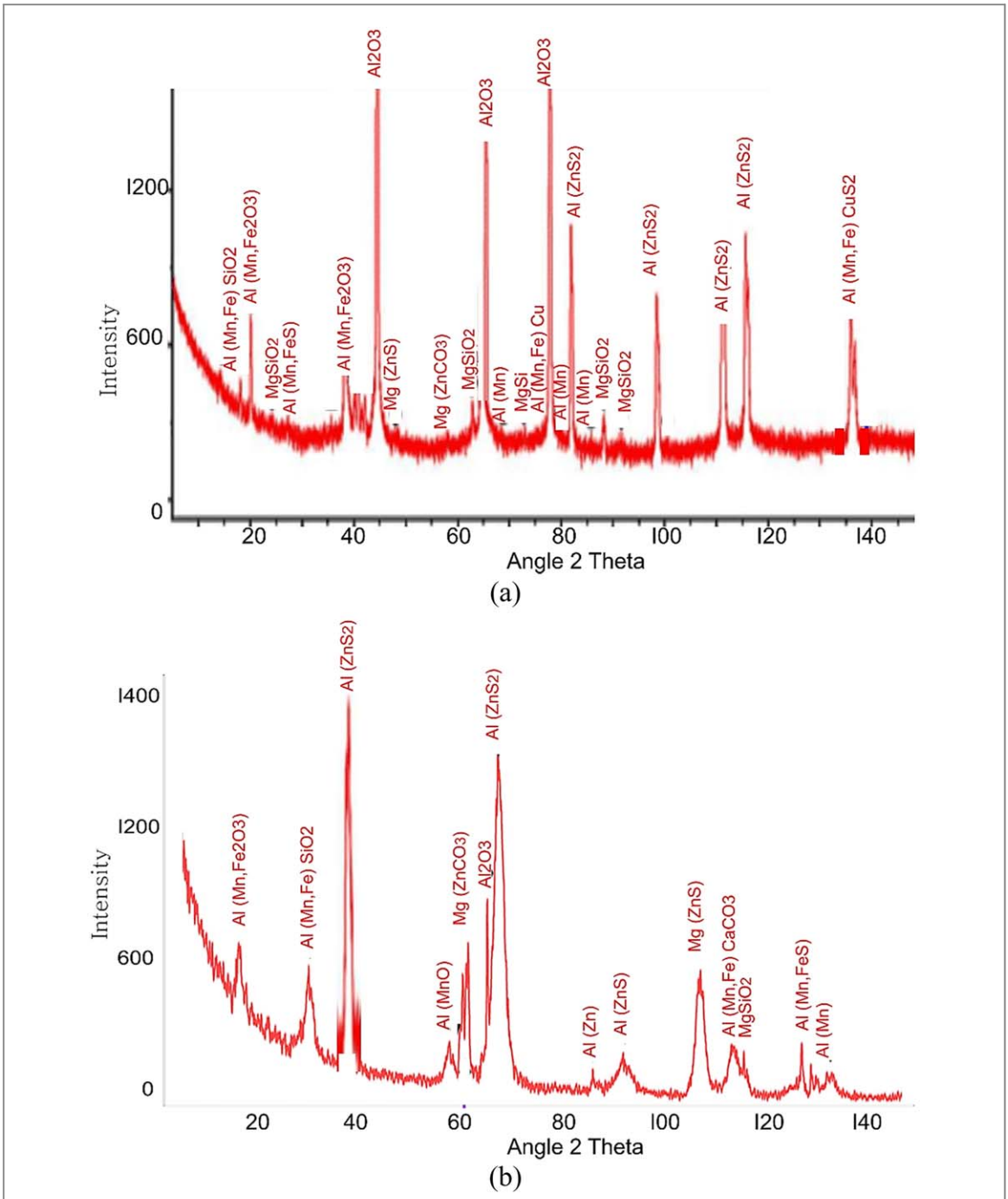

Figure 9. Representative XRD Phase identification plots for AA70/MH composite (sample E), (a) before corrosion and (b) after corrosion in 3.5% NaCl/0.0125 M H_2SO_4 solution.

Conclusion

Corrosion resistance of 1070 aluminium matrix composites reinforced with maize husk particulates at 5% and 15% wt. content, and 150 μm and 300 μm particle size was studied. The following conclusions were obtained from the research.

- Aluminium matrix composite at 5% wt. content and 150 um particle size of maize husk exhibited the least resistance to localized and corrosion from potentiodynamic polarization and weight loss analysis in chloride, sulphates and chloride-sulphate solution compared to the monolithic aluminium alloy and other composite fractions.
- Corrosion occurred marginally along the grain boundaries in chloride solution in addition to formation of micro-pits and scattered whitish precipitates.

- In sulphates solution, the extent of corrosion along the grain boundaries was much higher coupled with general surface deterioration. However, in the combined chloride-sulphate solution, total surface degradation was observed.
- Increase in maize husk weight content and particle size progressively decreased the corrosion vulnerability of the composite wherewith maize husk at highest weight content of 15% and 300 um particle size exhibited the lowest corrosion rate values obtained.
- Weight loss plots from chloride and sulphate solution showed significant increase in corrosion before relative stability compared to the plots from chloride-sulphate solution where significant decrease in corrosion was observed before relative stability.
- Open circuit potential plots showed significant potential transients in chloride and chloride-sulphate solution coupled with thermodynamic corrosion tendencies compared to the sulphate solution which where the transients were comparatively fewer.
- X-ray diffraction patterns showed significant variation between the corroded and non-corroded composites samples, and between the composite samples with respect to maize husk weight content and particle size in aluminium matrix.

Acknowledgments

The authors are grateful to Covenant University for their financial support towards this investigation.

Data availability statement

All data that support the findings of this study are included within the article (and any supplementary files).

Conflict of interest

Authors state no conflict of interest exists.

ORCID iDs

Roland Tolulope Loto https://orcid.org/0000-0002-1675-8989

References

[1] Nturanabo F, Masu L and Kirabira J B 2019 *Novel Applications of Aluminium Metal Matrix Composites* ed K O Cooke (ed) (London: Aluminium Alloys and Composites, IntechOpen) (https://doi.org/10.5772/intechopen.86225)
[2] Pouraliakbar H, Hosseini Monazzah A, Bagheri R, Seyed Reihani S M, Khalaj G, Nazari A and Jandaghi M R 2014 Toughness prediction in functionally graded Al6061/SiCp composites produced by roll-bonding *Ceram* **40** 8809–25
[3] Mavhungu S T, Akinlabi E T, Onitiri M A and Varachia F M 2017 Aluminum matrix composites for industrial use: advances and trends *Procedia Manuf* **7** 178–82
[4] Surappa M K 2003 Aluminium matrix composites: challenges and opportunities *Sadhana* **28** 319–34
[5] Rupa D 2012 Aluminium alloy-based metal matrix composites: a potential material for wear resistant applications *Int. Sch. Res. Notices* 594573 (https://doi.org/10.5402/2012/594573)
[6] Chakrapani P and Suryakumari T S A 2021 Mechanical properties of aluminium metal matrix composites-A review *Mater. Today* **45** 5960–4
[7] Vineeth K and Jayahari L 2018 Study of mechanical properties and wear behaviour of aluminium 6063 matrix composites reinforced with steel machining chips *Mater. Today* **5** 20285–91
[8] Pramanik P 2016 Effects of reinforcement on wear resistance of aluminum matrix composites *Trans. Nonferrous Met. Soc. China* **26** 348–58
[9] Pramod S L, Bakshi S R and Murty B S 2015 Aluminum-based cast *in situ* composites: a Review *J. Mater. Eng. Perform.* **24** 2185–207
[10] Narayana Murty S V S, Nageswara Rao B and Kashyap B P 2003 On the hot working characteristics of 6061Al–SiC and 6061–Al_2O_3 particulate reinforced metal matrix composites *Compos. Sci. Technol.* **63** 119–35
[11] Yang Z, Fan J, Liu Y, Nie J, Yang Z and Kang Y 2021 Strengthening and weakening effects of particles on strength and ductility of SiC particle reinforced Al-Cu-Mg alloys matrix composites *Materials* **14** 1219
[12] Barbara P, Dante P and Cataldo T 2008 Application of traditional investment casting process to aluminium matrix composites *Compos Part A Appl. Sci. Manuf.* **39** 1606–17
[13] Sanjeev D, Siddhartha D and Karabi D 2007 Abrasive wear of zircon sand and alumina reinforced Al–4.5 wt% Cu alloy matrix composites—A comparative study *Compos. Sci. Technol.* **67** 746–51
[14] Rajan T P D, Pillai R M, Pai B C, Satyanarayana K G and Rohatgi P K 2007 Fabrication and characterisation of Al–7Si–0.35Mg/fly ash metal matrix composites processed by different stir casting routes *Compos. Sci. Technol.* **67** 3369–77

[15] Ayar M S, George P M and Patel R R 2021 Advanced research progresses in aluminium metal matrix composites: An overview *AIP Conf. Proc.* **2317** 020026
[16] Md Ali A, Omar M, Hashim H, Salleh M and Mohamed I 2021 Recent development in graphene-reinforced aluminium matrix composite: A review *Rev. Adv. Mater. Sci.* **60** 801–17
[17] Su J and Teng J 2021 Recent progress in graphene-reinforced aluminum matrix composites *Front Mater Sci.* **15** 79–97
[18] Hidalgo-Manrique P, Yan S, Lin F, Hong Q, Kinloch I A, Chen X, Robert R J, Zhang X and Shenglong Dai S 2017 Microstructure and mechanical behaviour of aluminium matrix composites reinforced with graphene oxide and carbon nanotubes *J. Mater. Sci.* **52** 13466–77
[19] Asthana R, Singh M and Sobczak N 2005 The role of wetting and reactivity in infiltration of ceramic–metal composites *Ceram. Eng. Sci. Proc.* **26** 249–61
[20] Vassel A 1999 Continuous fibre reinforced titanium and aluminium composites: A comparison *Mater. Sci. Eng. A* **263** 305–13
[21] Rajan T P D, Pillai R M and Pai B C 1998 Reinforcement coatings and interfaces in aluminium metal matrix composites *J. Mater. Sci.* **33** 3491–503
[22] Rodel J, Prielipp H, Knechtel M and Claussen N 1994 Better ceramics through metal modification *Trans. Mater. Res. Soc. Jpn* **19B** 763–76 (https://mrs-j.org/pub/tmrsj/vol19B/vol19B_763.pdf)
[23] Schiroky G H, Fareed A S, Sonuparlak B, Lee C T and Sorenson B W 1992 Fabrication and properties of fiber-reinforced ceramic composites made by directed metal oxidation ed S R Levine *Flight- Vehicle Materials, Structures, and Dynamics* vol 3 (ASME) 151–63
[24] Trowsdale A J, Noble B, Harris S J, Gibbins I S R, Thompson G E and Wood G C 1996 The monitoring of the formation and destruction of corrosion inhibitor films using electrochemical noise analysis (ENA) *Corros. Sci.* **38** 177
[25] ASM Handbook 2001 *Composites* vol. 21
[26] ASM Handbook 1992 *Corrosion* vol 13 4th edn
[27] Paciej R C and Agarwala V S 1986 Metallurgical variables influencing the corrosion susceptibility of a powder metallurgy aluminum/SiC composite *Corrosion* **42** 718–29
[28] ASM Handbook 1992 *Corrosion* vol 13 4th edn
[29] Sambathkumar M, Sasikumar K S K, Gukendran R, Dineshkumar K, Ponappa K and Harichandran S 2021 Investigation of mechanical and corrosion properties of Al 7075/Redmud metal matrix composite *Rev. Metal.* **57** e185
[30] Liu J, Chen Z, Zhang F, Ji G, Wang M, Ma Y, Ji V, Zhong S, Wu Y and Wang H 2018 Simultaneously increasing strength and ductility of nanoparticles reinforced Al composites via accumulative orthogonal extrusion process *Mater. Res. Lett.* **6** 406–12
[31] Shi W, Yuan L, Xu F, Zheng Z and Shan D 2018 Refining whisker size of 2024Al/Al18B4O33w composite through extrusion and its effects on the material's micro-structures and mechanical properties *Mater. Charact.* **138** 98–106
[32] Kumar S N, Keshavamurthy R, Haseebuddin M R and Koppad P G 2017 Mechanical properties of aluminium-graphene composite synthesized by powder metallurgy and hot extrusion *Trans. Indian Inst. Met.* **70** 605–13
[33] Obi E R, Oguocha N A and Evitts R W 2007 Effect of fly ash reinforcement on the corrosion NaCl solution, Computational Methods and Experiments in Materials Characterisation III *WIT Trans. Eng. Sci.* **57** 21–30 (https://witpress.com/Secure/elibrary/papers/MC07/MC07003FU1.pdf)
[34] Rajesh M, Sharma K V, Shivarudraiah and Mahesha C R 2018 Corrosion Behavior Studies of Al7075 reinforced with multiwalled carbon nanotubes metal matrix composites in acidic medium *Int. J. Appl. Eng. Res.* **13** 10897–904 (https://ripublication.com/ijaer18/ijaerv13n12_109.pdf)
[35] Abdul Jameel A, Nagaswarupa H P and Krupakara P V 2010 Corrosion behaviour of Al 6061/Zircon metal matrix composites in alkali medium by open circuit potential studies *Asian J. Chem.* **22** 3910–6
[36] Mamatha M, Krupakara P V and Sreenivasa K 2020 Corrosion Characterization of Aluminium 7075 / Red Mud Metal Matrix Composites *IOSR J. Appl. Chem.* **8** 7–11
[37] Narayanan S, Sozhamannan G G, Hemalatha K, Velmurugan K and Venkatachalapathy V S K 2021 Corrosion and hardness behaviour of Al/GO nanocomposites processed by the ultrasonic gravitational stir casting method *Int. J. Corros.* **2021** 6658186
[38] Naresh M and Siva K 2020 investigation of microstructural, Mechanical and corrosion properties of AA7010-TiB_2 in-situ metal matrix composite *Sci. Eng. Compos.* **27** 97–107
[39] Roseline S and Paramasivam V 2019 Microstructural and corrosion aspects of aluminum-zirconia metal matrix composites in acidic condition *SSRG Int. J. Mech. Eng.* **6** 19–23
[40] Shargh S F, Saadat A, Najafi A, Gharehshiran M R K and Khalaj G 2020 Investigating the effect of post weld heat treatment on corrosion properties of explosive bonded interface of AA5083/AA1050/SS 321 tubes *Mater. Res. Express* **7** 036529
[41] Jandaghi M R, Saboori A, Khalaj G and Khanzadeh Ghareh Shiran M 2020 Microstructural evolutions and its impact on the corrosion behaviour of explosively welded Al/Cu bimetal *Metals* **10** 634
[42] Mendes C, Adnet F, Leite M, Furtado C G and Sousa A 2015 Chemical, physical, mechanical, thermal and morphological characterization of corn husk residue *Cellul. Chem. Technol.* **49** 727–35 (https://cellulosechemtechnol.ro/pdf/CCT9-10(2015)/p.727-735.pdf)
[43] Baeck Y and Frankel G S 2003 Electrochemical quartz crystal microbalance study of corrosion of phases in AA 2024 *J. Electrochem. Soc.* **150** B1–9
[44] Serdechnova M, Volovitch P, Brisset F and Ogle K 2014 On the cathodic dissolution of Al and Al alloys *Electrochim. Acta* **124** 9–16
[45] Reena K, Nayak J and Nityanand S 2016 Corrosion behavior of 6061/Al-15 vol. pct. SiC(p) composite and the base alloy in sodium hydroxide solution *Arabian J. Chem.* **9** S1144–54
[46] Loto R T and Adeleke A 2016 Corrosion of aluminum alloy metal matrix composites in neutral chloride solutions *J. Fail. Anal. Prev.* **16** 874–85
[47] Foley R T and Nguyen I H 1982 The chemical nature of aluminum corrosion V. Energy transfer in aluminum dissolution *J. Electrochem. Soc.* **129** 464–7
[48] Bennour I, Maurice V and Marcus P 2010 X-ray photoelectron spectroscopy study of the interaction of ultra-thin alumina films on NiAl alloys with NaCl solutions *Surf & Interf Analy* **42** 581–7
[49] Nguyen T H and Foley R T 1979 On the mechanism of pitting of aluminum *J. Electrochem. Soc.* **126** 1855–60
[50] Trowsdale A J, Noble B, Harris S J, Gibbins I S R, Thompson G E and Wood G C 1996 The influence of silicon carbide reinforcement on the pitting behaviour of aluminium *Corros. Sci.* **38** 177–91
[51] Feng Z, Lin C, Lin J and Luo J 1998 Pitting behavior of SiC /2024 Al metal matrix composites *J. Mater. Sci.* **33** 5637–42